Fullerenes, Nanotubes and Carbon Nanostructures

ISSN: 1536-383X (Print) 1536-4046 (Online) Journal homepage: http://www.tandfonline.com/loi/lfnn20

A new perspective on carbon nano-onion/nickel hydroxide/oxide composites: Physicochemical properties and application in hybrid electrochemical systems

Diana M. Bobrowska, Krzysztof Brzezinski, Luis Echegoyen & Marta E. Plonska-Brzezinska

To cite this article: Diana M. Bobrowska, Krzysztof Brzezinski, Luis Echegoyen & Marta E. Plonska-Brzezinska (2017) A new perspective on carbon nano-onion/nickel hydroxide/oxide composites: Physicochemical properties and application in hybrid electrochemical systems, Fullerenes, Nanotubes and Carbon Nanostructures, 25:3, 193-203, DOI: 10.1080/1536383X.2016.1267151

To link to this article: http://dx.doi.org/10.1080/1536383X.2016.1267151

Accepted author version posted online: 23 Feb 2017.
Published online: 23 Feb 2017.

FULLERENES, NANOTUBES AND CARBON NANOSTRUCTURES
2017, VOL. 25, NO. 3, 193–203
http://dx.doi.org/10.1080/1536383X.2016.1267151

Taylor & Francis
Taylor & Francis Group

A new perspective on carbon nano-onion/nickel hydroxide/oxide composites: Physicochemical properties and application in hybrid electrochemical systems

Diana M. Bobrowska[a], Krzysztof Brzezinski[a], Luis Echegoyen[b], and Marta E. Plonska-Brzezinska[a]

[a]Institute of Chemistry, University of Bialystok, Bialystok, Poland; [b]Department of Chemistry, University of Texas at El Paso, El Paso, Texas, USA

ABSTRACT

Carbon nano-onion (CNO) and $Ni(OH)_2$ or NiO composites were prepared by chemical loading of $Ni(OH)_2$ on the carbon surface. The samples were characterized by transmission electron microscopic (TEM) and scanning electron microscopic (SEM) methods, powder X-ray diffraction (XRD) technique and by differential-thermogravimetric analyses (TGA-DTG). The porosity properties were characterized by using nitrogen gas adsorption analyses. Pristine inorganic samples of NiO and $Ni(OH)_2$ revealed different morphologies and porous characteristics when compared to those of the CNO composites, which showed unique electrochemical properties. The electrochemical performance of the CNO/$Ni(OH)_2$ or CNO/NiO composites is largely affected by the mass, the morphology, the crystal phases of the inorganic component and the distribution of the $Ni(OH)_2$/NiO phase. The CNO composites were used as materials for hybrid charge-storage devices.

ARTICLE HISTORY
Received 10 October 2016
Accepted 28 November 2016

KEYWORDS
composites; carbon nano-onions; nanostructures; electrochemical measurements; impedance spectroscopy

1. Introduction

In past decades, various carbon-metal oxide composite electrodes have been developed by combining metal oxides and different carbon nanostructures, such as carbon nanotubes, carbon nanofibers, graphene, and reduced graphene oxides (1, 2). These materials are used for creating energy storage systems. Among various systems, electrochemical capacitors are the most popular (3,4). Three kinds of electroactive materials for capacitors have been developed, which are based on two different energy storage mechanisms (5). One type is electrochemical double layer capacitors (EDLC), in which the energy storage is achieved by charge accumulation at the electrode/electrolyte interface (6). Another type, called pseudocapacitors, are based on fast and reversible redox reactions of the electroactive materials (7). The term "pseudo" was created to describe electrodes that behaves like a capacitor (e.g., RuO_2, MnO_2), (8). These electrodes exhibit a linear dependence of the charge stored with the width of the potential window. Pseudocapacitors show larger capacitances than EDLCs. Nevertheless, their low conductivity leads to lower electron transport rates (9). The third type of energy-storage device is based on Faradaic reactions. In this case the charge accumulation is strongly dependent on electrode potentials. They have limited energy density because of low operating voltages in aqueous electrolytes (ca. 1 V (10)) and stability issues related to carbon oxidation (11). This is the disadvantage of these materials, in which energy storage is done by a chemical reaction rather than by physical interactions. In view of the above, these electrodes have a significantly higher specific energy, but are somewhat limited in other respects, like life-stability and repeatability.

Transition metal oxides constitute the major type of electrode materials these days (12). Several reports have shown that bare metal oxide electrodes can deliver large specific capacitances and high energy densities at low scan rates, so they are not good for practical applications (13). The conductance of metal oxides is very low. The surface area and the pore size distributions are difficult to control in these types of materials. NiO and $Ni(OH)_2$ are often used as faradaic rechargeable battery-type electrodes. Electrodes of different porosities have been prepared under different synthetic conditions (14). The nickel hydroxide systems can exist in different crystal phases (i.e., α and β) and various morphologies. α- and β-$Ni(OH)_2$ have the same hexagonal layered structure between the brucite layers (15). α-$Ni(OH)_2$ exhibits superior electrochemical properties because of the presence of intercalated water and anionic species (15). Many nickel hydroxide nanostructures such as nanoplates, nanobelts, and nanoribbons can be fabricated using a variety of methods (15–18). The synthetic method utilized the structure of the new materials and their physicochemical properties, including electrochemical. For example, amorphous nickel hydroxide nanospheres have been prepared which exhibit very high specific capacitances, above 2000 F g^{-1} (16). Cao et al. synthesized nickel hydroxide nanoboxes with diameters between 450 and 500 nm, that showed excellent electrochemical properties and a very high specific capacitance (17, 18).

The term "hybrid capacitors" can be used when pairing two electrode with different charge-storage behavior (8). The electrochemical systems presented in this work involves hybridization of faradaic rechargeable battery-type electrodes (NiO, $Ni(OH)_2$ or composites including carbon nanostructures and

CONTACT Marta E. Plonska-Brzezinska mplonska@uwb.edu.pl Institute of Chemistry, University of Bialystok, K. Ciolkowskiego 1K , 15-245 Bialystok, Poland.

inorganic component) with a non-faradaic, double-layer type electrochemical capacitor electrodes (carbon nano-onions) (19). The combination of the two materials with different chemical properties can result in high-rate capability and porosities with better electrochemical performances (higher energy and power densities, long-term cycling stabilities) (20).

Carbon nano-onions (CNOs) can be successfully applied for double-layer type electrochemical capacitor electrode (21), because they have unusual microtexture characteristics and better mesoporous properties than other carbon materials (22). The Brunauer–Emmett–Teller (BET) specific surface areas of CNOs determined by nitrogen gas adsorption analyses are between 380 and 600 $m^2\ g^{-1}$ (23), and their conductivity is similar to those of carbon black and graphitic structures (24). Therefore, CNOs used as electrode materials show constant capacitances over a large scan range (25). These structures are relatively small (diameters <10 nm) and spherical nanoparticles, that constitute zero-dimensional materials (0-D) (26). CNOs consist of a multilayered arrangement of closed fullerene shells with a distance between the layers of 0.335 nm (27). CNOs have been applied in electronics (28, 29), in energy conversion and storage (32–34), in catalysis (33), as cathodes in Li-ion electrochemical energy storage devices (34), as optical limiting agents (35, 36), as hyperlubricants (37, 38), as electron field emitters (39), and for biosensors (40).

Herein, we report a simple method for the preparation of composites of α-$Ni(OH)_2$ or NiO with CNOs. We successfully used these hybrid electrodes to improve the performance of our charge-storage devices.

2. Materials and methods

2.1. Materials

All chemicals and solvents used were commercially available and were used without additional purification: nickel(II) nitrate hexahydrate (>97.0%, Sigma-Aldrich), ethanol (99.8%, POCh), ammonium hydroxide (25%, POCh), conductive carbon paint—a dispersion of colloidal graphite (20% solids) in isopropyl alcohol, (4-dimethylamino)pyridine (4-DMAP) (99.0%, Sigma-Aldrich), and nanodiamond (ND) powder (Carbodeon μDiamond®Molto) with a crystal size between 4 and 6 nm, and ND content ≥97 wt.%. CNOs were produced in accordance with the procedure we have already published (41). Annealing of ultradispersed nanodiamonds was performed in an Astro carbonization furnace at 1650°C under a 1.1 MPa He atmosphere with a heating ramp of 20°C min^{-1}. The final temperature was maintained for 1 hour, then the material was slowly cooled down to room temperature over a period of one hour. The furnace was opened, and the CNOs were annealed in air at 400°C to remove any amorphous carbon. All aqueous solutions for electrochemical studies were made using deionized water, which was further purified with a Milli-Q system (Millipore).

2.2. Preparation of the CNO/$Ni(OH)_2$ and CNO/NiO composites with a different mass ratio

Ten milligrams of CNOs was dispersed in 1 mL of anhydrous ethanol, sonicated, and the resulting suspension was mixed with 1 mL of an aqueous solution of (4-dimethylamino)pyridine (20 mM) and stirred. Afterwards, different masses of nickel nitrate hexahydrate were added and then, a 5% ammonium hydroxide solution was added to the suspension dropwise until the pH reached 9.5. The composite material was obtained by centrifugation after washing several times with ethanol before drying overnight at 60°C in an oven. The CNO/$Ni(OH)_2$ composites with mass ratios of CNOs to $Ni(OH)_2$ of about 1:4, 1:3, and 1:1.5 were prepared. Subsequently, the CNO/NiO composites were obtained by calcination of the corresponding CNOs/$Ni(OH)_2$ at 400°C for 2 hours in an air atmosphere.

2.3. Methods

The materials were imaged by secondary electron scanning electron microscopy (SEM) using a FEI Tecnai S-3000N (Tokyo, Japan). The accelerating voltage of the electron beam was either 20 or 30 keV. Transmission Electron Microscopic images were recorded using the FEI Tecnai™ instrument (Tokyo, Japan). The accelerating voltage of the electron beam was 200 keV, the TEM point resolution was 0.25 nm, the TEM line resolution was 0.144 nm, the maximum diffraction angle was ±12°, and the working distance was 10 mm. The energy dispersive X-ray spectroscopy (EDX) analyses were performed with the ASPEX System, fully integrated and automated with the scanning electron microscope (S-3000N). Thermogravimetric experiments were performed using a SDT 2960 simultaneous TGA-DTG (TA Instruments company). The thermogravimetric spectra were recorded at 10°C min^{-1} in an air atmosphere (100 mL min^{-1}). The powder diffraction data were measured at 293 K using a SuperNova diffractometer (Agilent) with a CCD detector and a Cu-Kα radiation at 148 mm sample-to-detector distance. Prior to the experiment, all samples were loaded into capillaries with a diameter of 0.5 mm. N_2 gas adsorption measurements were performed using a Micromeritics apparatus (ASAP2020 - automatic sorption analyzer, Micromeritics Corp., USA) at –196°C. Prior to gas adsorption analysis, the samples were degassed at 350°C (including NiO) and at 120°C (including $Ni(OH)_2$) under low vacuum (10 μm Hg) for 20 hours to remove any adsorbed species.

The electrochemical measurements were performed using a computer-controlled Autolab modular electrochemical system equipped with a PGSTAT 12 potentiostat (Eco Chemie Utrecht, The Netherlands), using the NOVA 1.7 software (Eco Chemie Urtecht) and a three-electrode cell configuration. The working electrode was a glassy carbon (GC) disk electrode (Bioanalytical System Inc.) with a disk diameter of 2.0 mm. Prior to the measurements, the surface of the glassy carbon electrode was polished using 3.0 μm fine diamond polish and 1.0 μm micropolish alumina (Buehler) on Texmet/alumina pad (BASi). Afterwards, the GC electrode was immersed in ethanol, sonicated for a few minutes to remove the traces of alumina from the surface, washed with ethanol and dried. The film on the GC electrode was prepared as follows: 2 mg of an active material was dissolved in a solution containing conductive carbon paint and ethanol in a volume ratio of 1:6 and sonicated for 15 minutes. Subsequently, the surface of the working

electrode was modified by the drop-coating method. 10 μL of the CNO/$Ni(OH)_2$ or CNO/NiO solution was then transferred to the GC (1.5 mm diameter) surface and solvent was evaporated under an argon atmosphere. A saturated calomel electrode was used as reference electrode. The counter electrode was made from platinum mesh (0.25 mm). All experiments were done in water purified in a Millipore apparatus and saturated with in argone gas.

3. Results and discussion

3.1. Characterization of the CNO/$Ni(OH)_2$ and the CNO/NiO composites

The chemical composition, microstructure, and physical properties of the metal oxide/carbon composites determine the properties of the corresponding supercapacitor electrodes. To date, there are many report of the synthesis of 3D nano- and micro-structured $Ni(OH)_2$ and NiO composites (42). Using the same procedures as in our previous studies (43), we prepared the hybrid CNO/$Ni(OH)_2$ or CNO/NiO composites with varying weight ratios, following these reactions (14):

$$Ni^{2+} + NH_3{\cdot}H_2O \rightarrow \left[Ni(NH_3)_y\right]^{2+} + yH_2O \quad (1)$$

$$\left[Ni(NH_3)_y\right]^{2+} \rightarrow Ni^{2+} + yNH_3 \quad (2)$$

$$Ni^{2+} + 2OH^- \rightarrow Ni(OH)_2\downarrow \quad (3)$$

The synthesis was carried out in the presence of (4-dimethylamino)pyridine (4-DMAP) as a modifier, which promotes good dispersion of the CNOs (43), and resulted in homogenous composites. The amount of $Ni(OH)_2$ deposited on the carbon nanostructure surface can be easily controlled by the initial concentration of nickel sulfate. NiO was obtained by annealing the as-prepared $Ni(OH)_2$ at 400°C for 2 hours, according to Eq. (4):

$$Ni(OH)_2 \xrightarrow{\text{endothermic}} NiO + H_2O \quad (4)$$

The XRD patterns of $Ni(OH)_2$, NiO, pristine CNOs and their composites are presented in Figure 1. For all patterns, an asymmetric broad peak in the range between 21° and 27° and a second peak with a maximum at 43.0° were observed, that are attributed to the (002) and (100) planes of graphite (Figure 1a), respectively (44). For pristine $Ni(OH)_2$, the peaks appear at $2\theta = 12.2°$, 24.5°, 33.2°, and 59.2°, and correspond to the (003), (006), (101), and (110) planes of hexagonal α-$Ni(OH)_2$, respectively (Figure 1a, panel (1)). These data are in agreement with the reported standard values (JCPDS card No. 38-0715) (15). The low angle diffraction peaks attributed to the (003) and (006) planes indicate a layered structure in α-$Ni(OH)_2$ (45). The (003) peak intensity observed is much stronger than for the other peaks. The higher content of the inorganic component results in an increase of the spacing in the [001] direction (45). This phenomenon is observed as a shift of the peaks corresponding to the (003) and (006) planes to lower angles (10.8° and 20.1°, respectively) (Figure 1e, panel (1), triangle marked) (46). This effect could be attributed to an increasing amount of the

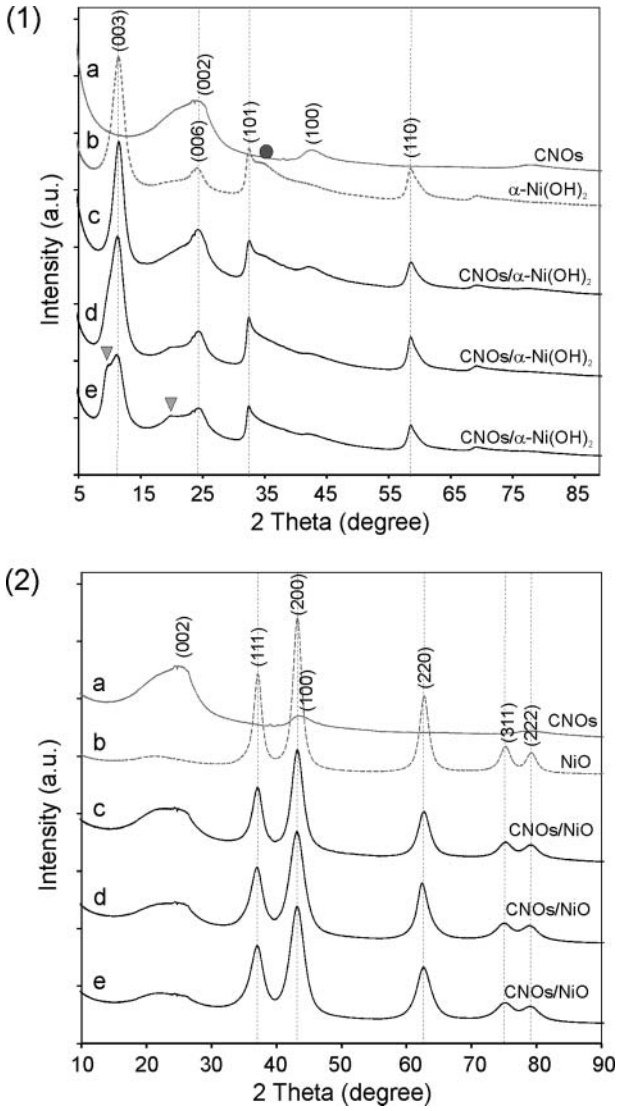

Figure 1. XRD patterns of (a) pristine CNOs; (1) $Ni(OH)_2$ sample of (b) pristine, and CNO/$Ni(OH)_2$ composites with mass ratio (m_{CNOs}:$m_{Ni(OH)2}$): (c) 1:1.5, (d) 1:2, and (e) 1:4; (2) NiO samples of (b) pristine, and CNOs/NiO composites with mass ratio (m_{CNOs}:m_{NiO}): (c) 1:1.5, (d) 1:2, and (e) 1:4.

intercalated anions in the α-$Ni(OH)_2$ phase, or/and to the transformation of the α-$Ni(OH)_2$ into the β-$Ni(OH)_2$ phase (46). The asymmetric broad peak in the range between 34° and 38° is attributed to disorder in α-$Ni(OH)_2$ crystal lattice (Figure 1b, panel (1), circle marked) (46). The XRD pattern reveals that the CNOs/$Ni(OH)_2$ composites (1:4) could contain a mixture of the α-$Ni(OH)_2$ and β-$Ni(OH)_2$ phases in the sample.

The XRD patterns of pristine NiO and of the NiO/CNO composites are displayed in Figure 1, panel (2). The diffraction peaks at 2θ values of 36.9°, 43.0°, 62.2°, 75.1°, and 78.9°, correspond to the (111), (200), (220), (311), and (222) crystal planes, respectively. A thermal decay of α-$Ni(OH)_2$ to NiO is related to a change of symmetry from hexagonal to face-centered cubic (JCPDS No. 69-2901) (45). Because the intensity of the (200) diffraction peak is higher than the others, it can be deduced that the boundary faces of the NiO phase are mainly the [100] surfaces (46).

Differential-thermogravimetric analyses (TGA-DTG) were performed to analyze the thermal stability of the pristine CNOs and their nickel composites in an air atmosphere. Figure 2

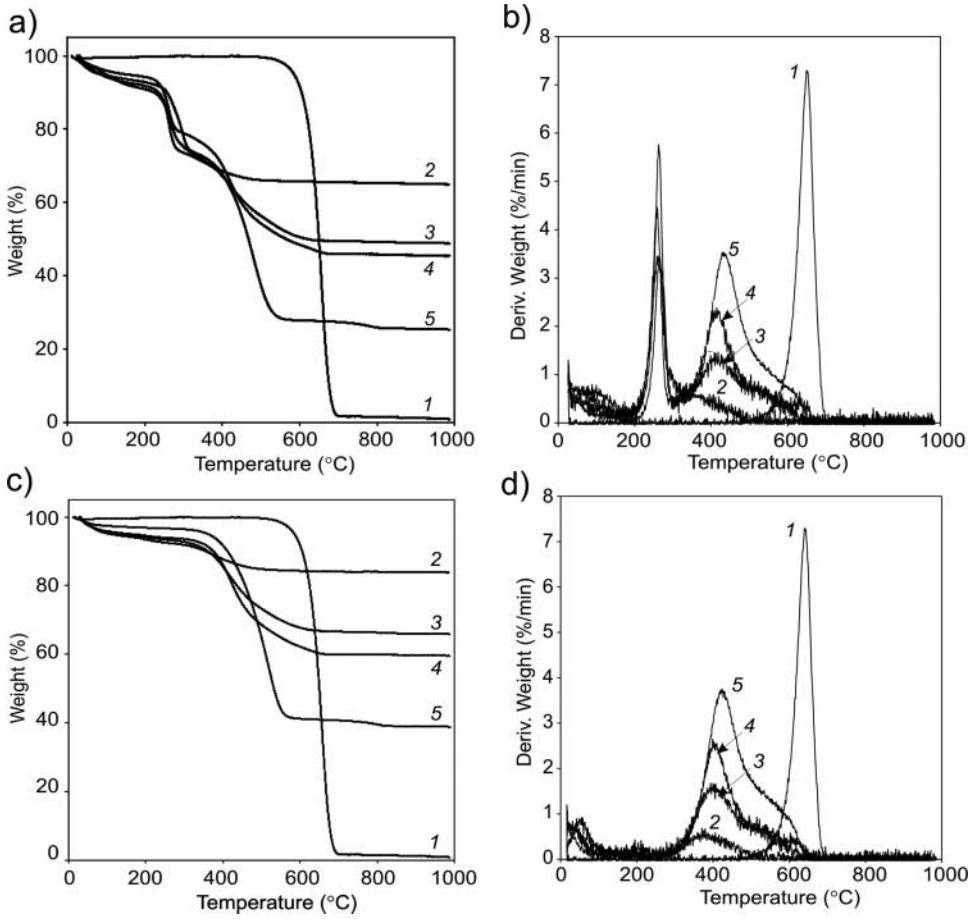

Figure 2. (a, c) TGA curves for (a) $Ni(OH)_2$ or (c) NiO and their composites with CNOs with different mass ratio (3) 4:1, (4) 3:1, (5) 1.5:1, and (1) CNOs and (2) plain inorganic component. (b, d) DTG curves for (b) $Ni(OH)_2$ or (d) NiO and their composites with CNOs with different mass ratio (3) 4:1, (4) 3:1, (5) 1.5:1, and (1) CNOs and (2) plain inorganic component. Measurements made in an air atmosphere at 10°C min^{-1}.

shows the TGA-DTG curves recorded up to 1000°C at 10°C min^{-1}. The onset of oxidation, inflection and end temperatures, total weight loss are listed in Table 1, corresponding to initial weight loss, the maximum weight loss and the final weight in the TGA-DTG graphs, respectively. The highest inflection temperature was observed for the pristine CNOs, I_t = 650°C (Table 1, Figure 2 curves (1)), with a total weight loss of 98% up to 700°C (Table 1). The single sharp mass loss transition corresponding to the combustion of CNOs signifies that the material is a homogeneous single phase with no other carbon material impurities (Figures 2b and d, curve 1).

The percentage of NiO and $Ni(OH)_2$ in the composites can be estimated from the weight loss of the TGA curves. The uncalcinated products, $Ni(OH)_2$, and their composites contain both intercalated and adsorbed water molecules and the content may vary depending on the experimental conditions. Different amounts of water are present in the samples (see Figure 2a, curves 3, 4, and 5, for the CNO/$Ni(OH)_2$ composites with mass ratios: 1:4; 1:3, and 1:1.5 (Table 1)). Very sharp transitions are observed at 261°C and 408°C (Figures 2b and d), that correspond to the conversion of $Ni(OH)_2$ to NiO and H_2O (Figure 2a, curves: 2, 3, 4, 5) (47). The first peak is a result of o the removal of chemically adsorbed water. The complete loss of water, ~33%, was observed at 400°C (Figure 2a, curve 2). Based on the TGA results, we chose 400°C as the annealing temperature for the production of the NiO composite materials. The mass ratios of NiO to CNOs calculated from the TGA studies (Figure 2c), are similar to those determined for the $Ni(OH)_2$ composites: 1:4; 1:3, and 1:1.5 (Table 1).

Many efforts have been made to optimize composite morphologies to enable high specific capacitances and cycling stabilities (5, 48). The specific capacitance values correlate well with the nature of the electrode/electrolyte interface. The porous structure of the carbon materials determines the ionic conductivity, which results from the mobility of the ions inside the pores (3, 6, 7, 9). The porosity of the CNO/$Ni(OH)_2$ and the CNO/NiO composites and their reference materials (Ni

Table 1. The TGA-DTG-DTA parameters of substrates and composites.

Sample	Onset temperature (°C)	Inflection temperature (°C)	End temperature (°C)	Total weight loss (%)
CNO	500	650	700	98
$Ni(OH)_2$	200	261	490	33
NiO	280	408	490	15
CNO/Ni $(OH)_2$				
1:4	180	261, 408	690	52
1:3	180	261, 420	690	58
1:1.5	180	275, 440	680	71
CNO/NiO				
1:4	240	408	680	34
1:3	250	415	690	40
1:1.5	250	430	680	54

($(OH)_2$, NiO, and CNOs), were determined using N_2 adsorption/desorption isotherms (Table 2). The micro- and mesopore structures, the pore volumes and the specific surface areas of all samples were measured using a multilayer model of coverage adsorption, the BET static nitrogen adsorption method (49). Starting from the isotherm, it's possible to correlate the necessary gas volume to fill all the pores in the materials. The major pore size distribution for plain $Ni(OH)_2$, NiO, the CNO/NiO, and the CNO/$Ni(OH)_2$ composites was found to be in the range of 10–17 nm. The pore diameters define these materials as mesoporous. The BET specific surface areas (S_{BET}) were obtained from linear plots of $1/[Q(p/p^0)-1]$ versus the relative pressure (p/p^0), where Q is the weight of the adsorbed gas (6, 9, 50). An S_{BET} of 453 $m^2\ g^{-1}$ was obtained for plain CNOs, that is very close to the value for the ideal spherical solid particles of 5 nm size (51). Structures with a diameter of 5 nm corresponds to an S_{BET} valve of 343 and 545 $m^2\ g^{-1}$, based on the known density of diamond (3.5 g cm^{-3}) and for graphitic carbon (2.2 g cm^{-3}), respectively (51).

The S_{BET} values of the CNO/$Ni(OH)_2$ and the CNO/NiO composites range between 109 and 385 $m^2\ g^{-1}$. The smallest S_{BET} value was determined for the composite with the highest mass ratio of the inorganic component. The S_{BET} of plain $Ni(OH)_2$ and NiO were found to be 173 and 82 $m^2\ g^{-1}$, respectively. During calcination of $Ni(OH)_2$, hydroxyl groups are removed from the pore system and pore walls collapse, which causes the BET surface area, microporosity, and average pore size to decrease. Doping of the inorganic components with the CNOs resulted in the increase of their microporosity (Table 2), and the total surface area of the micropores increased from 23 $m^2\ g^{-1}$ (CNOs/NiO 1:1.5), or 20 $m^2\ g^{-1}$ (CNOs/$Ni(OH)_2$ 1:1.5) to 111 $m^2\ g^{-1}$ (plain CNOs) to indicating that the structure of the pores changed dramatically for the microporous domain.

From the High-Resolution Transmission Electron Microscopy (HRTEM) images (Figures 3a and b), the CNO/$Ni(OH)_2$ composites consist of a large number of wrinkled surfaces (structure 2). After calcination $Ni(OH)_2$ forms more regular granular structures (Figure 3b). HRTEM of the CNO composites (Figures 3a and b) showed both structures: the inorganic (structures 2 and 3) and the carbon particles (structure 1) in the composite matrix. The CNO/$Ni(OH)_2$ composites consist of a large number of wrinkled surfaces. SEM images of a Au foil covered with the CNO composites are shown in Figures 3 (c)–(h). The CNOs tend to agglomerate, which results from the van der Waals interactions between the nanoparticles (Figures 3d and e). The carbon nanoparticles provide high specific surfaces for the nucleation of $Ni(OH)_2$ nanoparticles that results in a homogeneous distribution of the inorganic phase on the CNO's surfaces (Figures 3d and f). After calcination $Ni(OH)_2$ forms more regular granular structures. The energy dispersive X-ray (EDX) spectra (Figures 3i and j) of the CNO composites reveal that the materials mainly contain C, O, and Ni, with different mass ratios of the inorganic to the organic phases.

Table 2. The porosity parameters of the CNO/NiO and the CNO/$Ni(OH)_2$ composites and of their reference compounds based on N_2 adsorption/desorption isotherms.

Sample	S_{BET}[a] ($m^2\ g^{-1}$)	Micropore Area[b] ($m^2\ g^{-1}$)	Pore Volume ($cm^3\ g^{-1}$)	Avarage pore size (nm)
CNO	453	111	1.44	14
$Ni(OH)_2$	173	19	0.75	17
CNO/$Ni(OH)_2$				
1:4	201	38	0.78	16
1:3	235	26	0.85	14
1:1.5	257	20	0.86	13
NiO	82	22	0.31	17
CNO/NiO				
1:4	109	41	0.88	10
1:3	225	27	0.71	14
1:1.5	385	23	0.40	16

[a] S_{BET} – BET specific surface area.
[b] Based on the t-plot method; single point adsorption total pore volume at relative $p/p^0 = 0.984$.

3.2. The electrochemical properties of the hybrid materials

The goal of this work is to develop materials for electrodes that simultaneously possess high energy densities, exhibit fast electron transfer rates and have long-term cycling stabilities (52). To demonstrate the advantages of hybrid electrodes $Ni(OH)_2$ or NiO with CNOs) which were `obtained by hybridization of faradaic with non-faradic materials, we have investigated the electrochemical properties of these materials in a three-electrode configuration cell. The working electrode was modified by a drop coating method, described in detail in the experimental section. The CV measurements of plain nickel hydroxide and oxide, and of the hybrid composites were performed at a sweep rate from 5 to 30 mV s^{-1} within a voltage window between −0.6 and 0.6 V vs. SCE in 1 mol L^{-1} KOH aqueous solution (Figure 4). Each CV curve consists of a pair of redox peaks and there is an increase in current with the scan rate. As the scan rate is increased, the cathodic and anodic peaks are shifted to more negative and positive potentials, respectively, as a consequence of the internal resistance of the films. This allows efficient ion transport at the interface of hybrid electrode and electrolyte. It is well-known that only the outer active sites can sustain redox reactions at high scan rates (53). The anodic sweeps of the CV curves are unsymmetric compared to the corresponding cathodic processes, that exhibit partial irreversibility (Figure 4). The hybrid devices involving Faradaic reactions exhibit polarization and ohmic resistance during the Faradaic process and thus ideal reversibility cannot be kinetically achieved for the positive and negative cycles (54, 55). The oxidation peak is a result of the conversion of $Ni(OH)_2$ or NiO to NiOOH, and the reduction peak corresponds to the reverse of this reaction. The redox reactions can be described as (54, 55):

$$NiO + zOH^- \leftrightarrows zNiOOH + (1-z)NiO + ze \quad (5)$$

$$Ni(OH)_2 + OH^- \leftrightarrows NiOOH + H_2O + e \quad (6)$$

where z is the number of active sites accessed by the OH^- (53).

The composites exhibit higher capacitive current than the component materials separately (Figure 5a). Incorporation of CNOs into the composites resulted in a significant improvement of the capacitive characteristics of the films through the formation of highly porous structures. The carbon nanostructures enable the diffusion of electrolyte to the interior of the films. Slower scan rates facilitate the access of hydroxyl ions

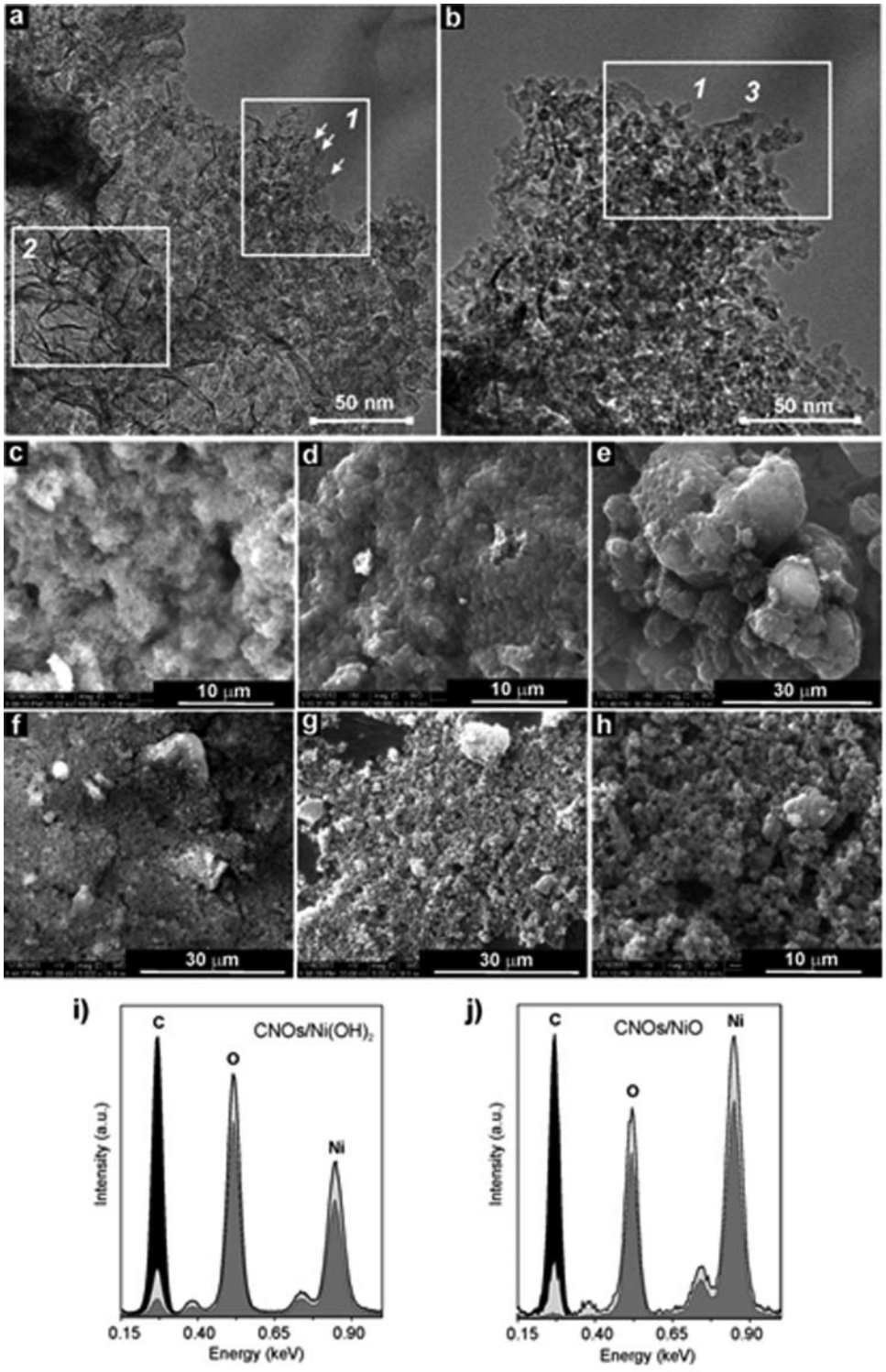

Figure 3. TEM images of the (a) CNOs/$Ni(OH)_2$, (b) CNOs/NiO composites of mass ratio 1:1.5. SEM images of the Au foil covered with (c) $Ni(OH)_2$, (d) NiO, (e) CNOs, and composites of (f) CNOs/$Ni(OH)_2$ (1:1.5), (g, h) CNOs/NiO (1:1.5). (i, j) EDX analysis of the (i) CNOs/$Ni(OH)_2$ and (j) CNOs/NiO composites with a different mass ratio.

into the films thus increasing the efficiency of the electrochemical reactions (Eqs 5 or 6). The higher capacitive current obtained for the composite electrodes indicate the synergistic effect between the inorganic components and the carbon materials. This can be attributed to the enhanced electrical conductivities and facilitated ion transport and diffusion.

In order to obtain practical applications with the new materials, the electrodes must exhibit reasonably high electrochemical cycling stability. Long cycling-life tests were conducted over 5000 cycles using the CNOs and CNO/$Ni(OH)_2$ composite electrodes (1 mol L^{-1} KOH) at a scan rate of 1 mV s^{-1}. The CNO/$Ni(OH)_2$ electrodes exhibit long-term cycling stability, retaining ca. 60% of their initial capacity after 5000 cycles within a 1.2 V voltage range (vs. Ag/AgCl).

At high scan rates, electrolyte ions cannot fully access the interior surfaces of the active materials for effective

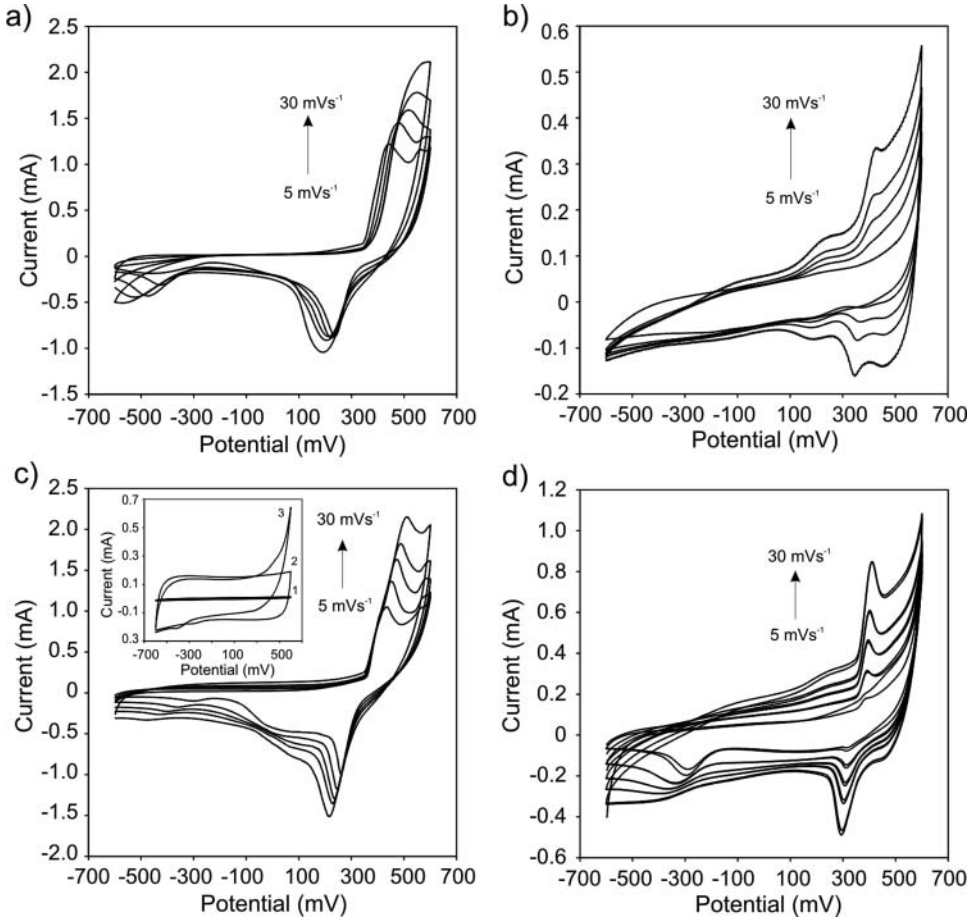

Figure 4. Cyclic voltammograms of a GC electrode in 1 M KOH covered with: (a) $Ni(OH)_2$, (b) NiO, (c) CNOs/$Ni(OH)_2$ (1:1.5) (Insert: CVs of a GC electrode covered with (*1*) carbon paste, (*2,3*) CNOs; (*2*) 0.1 mol L^{-1} NaCl, and (*3*) 1 mol L^{-1} KOH; v = 5 mV s^{-1} (45)), and (d) CNOs/NiO (1:1.5) with the different scan rates: 5, 10, 15, 20 and 30 mV s^{-1} and in a three-electrode system.

redox reactions. In order to verify this point the effect of the sweep rates on the anodic peak currents was investigated, as shown in Figure 5(a). The linear relationship of the plot of the peak currents (at the potential of anodic peaks) versus the slow sweep rates (below 30 mV s^{-1}; Figure 5a) indicate a fast electron transfer rate during the redox reaction in KOH solution and the electrode process is diffusion-controlled (56). When the sweep rate was increased to 30 mV s^{-1}, the capacitive current decreased and represented only ca. 60% of the starting value. However, the shapes of the CV curves remain essentially unchanged even at high scan rates, suggesting that the cells

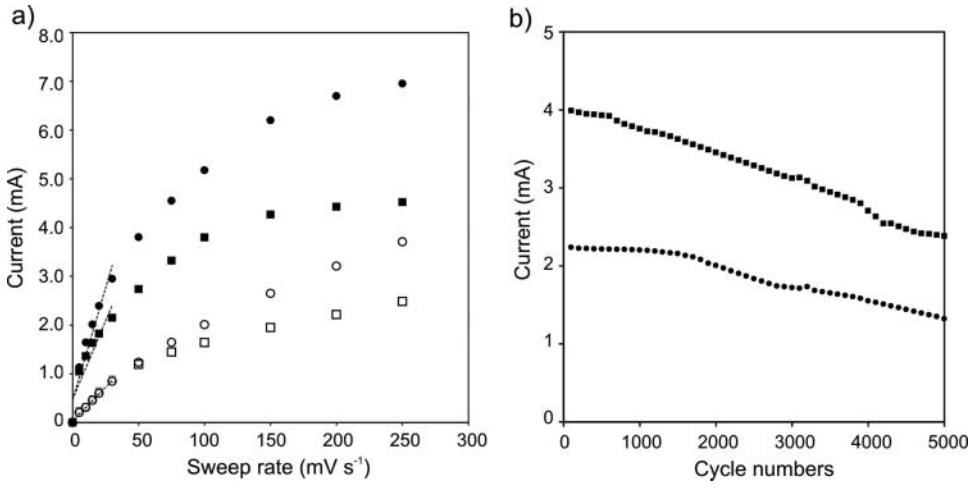

Figure 5. (a) Dependence of the capacitive current (at the potential of anodic peak) in a three-electrode system, with the sweep rate for: (●) CNOs/$Ni(OH)_2$ (1:3), (■) CNOs/$Ni(OH)_2$ (1:1.5), (□) CNOs/NiO (1:1.5), (○) CNOs/NiO (1:3). (b) Performances measured at a scan rate of 100 mV s^{-1} for 5000 cycles in 1 mol L^{-1} KOH of GCE covered with (■) CNOs/$Ni(OH)_2$ (1:4) and (●) CNOs/$Ni(OH)_2$ (1:1.5).

possess excellent rate capability, while the gravimetric capacitance decreased gradually upon increasing scan rates. There was a gradual decrease in the capacitive current with increasing the sweep rates. Nevertheless, the capacitive current of the CNO composites were always higher than those of the pristine inorganic materials at all scan rates (Figure 5a).

The electrochemical stabilities, capacitive properties of the layers, and the kinetics of the charging processes of the films were determined using the electrochemical impedance spectroscopy (EIS). Impedimmetric studies provide complementary information about the frequency response of electrode materials in supercapacitors and allow the estimation of capacitance changes with frequency (Figure 6) (6, 57). For composites containing redox active components, faradaic impedance spectra exhibit semicircular Nyquist plots due to charge transfer resistance, R_{CT}, at high frequencies, and a Warburg impedance range of linear Z'-Z'' (real-imaging impedance components) at medium frequencies (58). In the low-frequency range, a finite length effect (in the Z'-Z''plot) dominates the frequency response. The low-frequency capacitance, C_L, is described by the equation:

$$Z'' = \frac{1}{(j\omega C_L)} \tag{7}$$

where the specific capacitance, C_L, can be obtained from the slope of Z'' versus ω^{-1}. ω is the angular frequency which is given by $2\pi f$ (59).

It is well known that the complex form of the capacitance is frequency dependent, defined as follows (59):

$$C(\omega) = C'(\omega) - jC''(\omega) \tag{8}$$

where $C'(\omega)$ and $C''(\omega)$ are the real and imaginary parts of the complex capacitance $C(\omega)$, respectively. At low frequency, $C'(\omega)$ corresponds to the capacitance of the electrode materials and $C''(\omega)$ is a function of the energy dissipation by irreversible processes. Both capacitances are expressed as:

$$C'(\omega) = \frac{-Z''(\omega)}{\omega |Z(\omega)|^2} \tag{9}$$

$$C''(\omega) = \frac{Z'(\omega)}{\omega |Z(\omega)|^2} \tag{10}$$

From the Nyquist plots for the composites with a various mass ratios, it was possible to determine the influence of the particular components on the electrochemical properties of the electrode materials. The Nyquist plots were recorded in the frequency range between 0.1 and 10^5 Hz for all samples (Figure 6) and fitted using Scheme 1. The plots were composed of a linear segment at low frequencies and a semicircle at high frequencies (see Figure 6). The semicircle is associated with electrode surface properties and corresponds to the charge transfer resistance (R_{CT}) caused by the Faradaic reactions and the double layer capacitance at the surface (C_{DL}), that is a limiting factor for the rate of the supercapacitor (58). Figure 6 shows

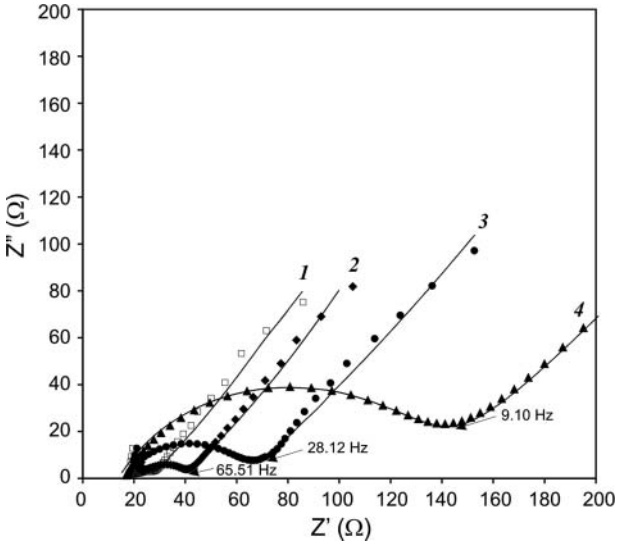

Figure 6. Nyquists plots (···) and data fits using the equivalent circuit shown in Scheme 1 (—) in 1 M KOH for the GC electrode covered with (*1*) $Ni(OH)_2$, (*2*) CNO/$Ni(OH)_2$ (1:1.5), (*3*) CNO/$Ni(OH)_2$ (1:3), (*4*) CNO/$Ni(OH)_2$ (1:4) at the potential of anodic peaks. Frequency was in the range of 100 kHz to 0.1 Hz, in a three-electrode system.

semicircle in the Nyquist plots of all CNO composites. A smaller semicircle implies better electrode/electrolyte interfacial ionic conductivity (60). The diameter of semicircle grows (Figures from 6b to d), when the inorganic content in the composites is increased. R_{CT} values increases with higher inorganic content. This suggests that the number of surface electrochemical reaction sites decreases with an increase in inorganic content. Excess of inorganic content blocks electrolyte ion diffusion channels into electrodes, resulting in higher R_{CT} and lower C_{DL}. The C_{DL} value reaches a maximum for CNO/$Ni(OH)_2$ (1:1.5). Higher CNO ratios in the composites enhanced the electrical conductivity and facilitated interfacial charge transfer at the electrode (Table 3). Furthermore, the composite electrodes containing CNOs exhibited improved durability.

The capacitive charge storage of the composites has contributions from both faradaic and double-layer effects. The separation of these effects was possible by applying different model to the EIS results. An equivalent circuit was used to fit the impedance spectra for the composites (Scheme 1). The values of the equivalent circuit parameters used for the simulations are collected in Table 3. Experimental impedance plots for the different hybrid materials were fitted well by the simulations with this equivalent circuit (see Figure 6). The solid curves represent the simulated Z'--Z'' responses. The equivalent series resistance (ESR) of the circuit included: a solution resistance (R_S), a charge transfer resistance (R_{CT}) for electron transfer at the electrode/electrolyte

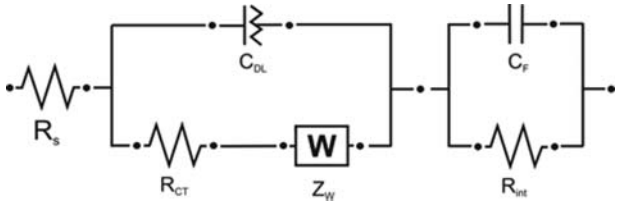

Scheme 1. The equivalent circuit used for fitting the EIS spectra.

Table 3. Electrochemical impedance parameters determined at the potential of anodic peaks applied to the 2 mm diameter GC electrode coated with the CNO/Ni(OH)$_2$ composites.

Sample CNO/Ni(OH)$_2$	R_s (Ω)	Estimated Error (%)	n	C_{DL} (mF)	Estimated Error (%)	R_{CT} (Ω)	Estimated Error (%)	Z_w (Ω)	σ (kΩ s$^{-1/2}$)	C_F (mF)	Estimated Error (%)	R_{int} (Ω)	C_s (F g^{-1})
1:4	15.3	24.1	0.60	0.064	13.5	110.0	13.5	91.7	0.82	191.0	9.1	250.0	**1120**
1:3	15.0	13.7	0.65	0.080	10.5	51.0	8.6	85.8	2.36	174.0	12.8	122.3	**1015**
1:1.5	22.4	12.5	0.75	0.095	18.4	16.5	15.8	74.1	3.16	112.0	36.0	93.6	**654**

interfaces, internal resistance of the CNO/Ni(OH)$_2$ composites (R_{int}), a double-layer capacitance (C_{DL}) due to the carbon component, and a faradaic capacitive behavior (C_F). A Warburg diffusion element (Z_W) due to diffusion of the ions to the electrode/electrolyte was also included (61, 62).

At low frequencies (1–0.01 Hz), the real part of the impedance reaches its limiting value. The Nyquist plot of a perfect capacitor with ideally polarizable electrodes should exhibit a straight line parallel to the imaginary axis (60). The n parameter is connected with C_{DL}. This parameter is close to unity for an ideal capacitor (an electrode with rough and porous electrode) and $n \leq 1$ for materials containing a redox component (63). The n parameter with values between 0.60 and 0.75 is characteristic for redox materials of composite electrodes (63). At higher frequencies, the changes of the phase angle are related to the faradaic processes of the electron transfer at the composite/electrode interphases. This region is correlated with a diffusion limit at the electrode. The Warburg coefficient, σ, can be determined from the Equation:

$$Z_W = \left(\frac{2}{\omega}\right)^{1/2} \sigma \tag{11}$$

where, Z_W is the total impedance and ω is the angular frequency ($\omega = 2\pi f$). The Warburg coefficients (σ) were determined in the range between 0.82 and 3.16 kΩ s$^{-1/2}$ for the CNO/Ni(OH)$_2$ composites. Another important parameter for electrode materials is the knee frequency (Figure 6). A high knee frequency is typical for high power capacitors (62). The knee frequency is defined as the value at which the lowest imaginary impedance is found or the frequency value at which the impedance starts to be dominated by its imaginary part (61). The studied composites had knee frequencies in the range between 65.51 and 9.10 Hz.

The capacitive properties depend on the total mass of the composites and on the mass of the inorganic components. The C_S values were evaluated from the semicircle in the EIS spectra, which represent the sum of the redox reactions (Ni^{2+}/Ni^{3+}) capacitance (C_F) and the electrical double layer capacitance (C_{DL}). The highest specific capacitance was found to be 1120 F g^{-1} for CNO/Ni(OH)$_2$ (1:4).

4. Conclusions

We have shown that carbon nano-onion composites with inorganic materials, such as Ni(OH)$_2$ or NiO, can be easily prepared. CNOs improve the composite film properties, promoting faradaic reactions, thus resulting in higher capacitances and better stabilities than pristine Ni(OH)$_2$ or NiO. The electrochemical performance of the composites is largely affected by the mass of the inorganic components, the morphology, the crystal phases of the inorganic component and the distribution of the Ni(OH)$_2$/NiO phase. The combination of CNOs with inorganic components results in homogeneous composites with long-term cycling stability due to the presence of the carbon nanoparticles. The CNO/Ni(OH)$_2$ composites exhibited high capacitance ca. 1120 F g^{-1} for thin films prepared by drop-coating. The CNO/Ni(OH)$_2$ electrodes exhibit also long-term cycling stability within 1.3 voltage range. Combination of the two types of materials improved the capacitive properties. These composites result in effective hybrid capacitive devices.

Acknowledgments

We gratefully acknowledge the financial support of the National Science Centre, Poland, grant #2012/05/E/ST5/03800 to M.E.P.-B. L.E. thanks the Robert A. Welch Foundation for an endowed chair, grant #AH-0033 and the US NSF, grants: DMR-1205302 (PREM Program) and CHE-1408865. SEM, TEM, XRD, AUTOLAB, and porosimeter were funded by European Funds for Regional Development and National Funds of Ministry of Science and Higher Education, as part of the Operational Programme Development of Eastern Poland 2007–2013, projects: POPW.01.03.00-20-034/09 and POPW.01.03.00-20-004/11.

References

1. Su, A. D., Zhang, X., Rinaldi, A., Nguyen, S. T., Liu, H., Lei, Z., Lu, L., and Duong, H. M. (2013) Hierarchical porous nickel oxide–carbon nanotubes as advanced pseudocapacitor materials for supercapacitors, *Chem. Phys. Lett.,* 561–562: 68–73. doi:10.1016/j.cplett.2013.01.023.
2. Yan, J., Sun, W., Wei, T., Zhang, Q., Fan, Z., and Wei, F. (2012) Fabrication and electrochemical performances of hierarchical porous Ni(OH)$_2$ nanoflakes anchored on graphene sheets, *J. Mater. Chem.,* 22: 11494–11502. doi:10.1039/C2JM30221G.
3. Inagaki, M., Konno, H., and Tanaike, O. (2010) Carbon materials for electrochemical capacitors, *J. Power Sources,* 195: 7880–7903.
4. Li, X. and Wei, B. (2013) Supercapacitors based on nanostructured carbon, *Nano Energy*, 2: 159–173.
5. Bose, S., Kuila, T., Mishra, A. K., Rajasekar, R., Kim, N. H. and Lee, J. H. (2012) Carbon-based nanostructured materials and their composites as supercapacitor electrodes, *J. Mater. Chem.,* 22: 767–784.
6. Kötz, R. and Carlen, M. (2000) Principles and applications of electrochemical capacitors, *Electrochimica Acta,* 45: 2483–2498.
7. Simon, P. and Gogotsi, Y. (2008) Materials for electrochemical capacitors, *Nat. Mater.*, 7: 845–854.
8. Brousse, T., Belanger, D., Long, J. W. (2015) To Be or Not To Be Pseudocapacitive?, *J. Electrochem. Soc.,* 162: A5185–A5189. doi:10.1149/2.0201505jes.
9. Frackowiak, E. and Beguin, F. (2001) Carbon materials for the electrochemical storage of energy in capacitors, *Carbon*, 39: 937–950.
10. Toupin, M., Bélanger, D., Hill, I. R., and Quinn, D. (2005) Performance of experimental carbon blacks in aqueous

supercapacitors, *J. Power Sources,* 140: 203–210. doi:10.1016/j.jpowsour.2004.08.014.
11. Zheng, J. P. (2003) The limitations of energy density of battery/double-layer capacitor asymmetric cells, *J. Electrochem. Soc.,* 150: A484. doi:10.1149/1.1559067.
12. Wang, D.-W., Li, F., and Cheng, H.-M. (2008) Hierarchical porous nickel oxide and carbon as electrode materials for asymmetric supercapacitor, *J. Power Sources,* 185: 1563–1568.
13. Lota, K., Sierczynska, A., and Lota, G. (2011) Supercapacitors based on nickel oxide/carbon materials composites, *Int. J. Electrochem.*, 2011: 1–6. doi:10.4061/2011/321473.
14. Yuan, C., Zhang, X., Su, L., Gao, B., and Shen, L. (2009) Facile synthesis and self-assembly of hierarchical porous NiO nano/micro spherical superstructures for high performance supercapacitors, *J. Mater. Chem.,* 19: 5772–5777.
15. Tong, G.-X., Liu, F.-T., Wu, W.-H., Shen, J.-P., Hu, X., and Liang, Y. (2012) Polymorphous α-and β-Ni $(OH)_2$ complex architectures: morphological and phasal evolution mechanisms and enhanced catalytic activity as non-enzymatic glucose sensors, *Cryst. Eng. Comm.*, 14: 5963–5973.
16. Li, H. B., Yu, M. H., Wang, F. X., Liu, P., Liang, Y., Xiao, J., Wang, C. X., Tong, Y. X., and Yang, G. W. (2013) Amorphous nickel hydroxide nanospheres with ultrahigh capacitance and energy density as electrochemical pseudocapacitor materials, *Nat. Commun.*, 4: 1894.
17. Fu, Y., Song, J., Zhu, Y., and Cao, C. (2014) High-performance supercapacitor electrode based on amorphous mesoporous Ni (OH) 2 nanoboxes, *J. Power Sources,* 262: 344–348.
18. Li, L., Xu, J., Lei, J., Zhang, J., McLarnon, F., Wei, Z., Li, N., and Pan, F. (2015) A one-step, cost-effective green method to in situ fabricate Ni (OH) 2 hexagonal platelets on Ni foam as binder-free supercapacitor electrode materials, *J. Mater. Chem. A.*, 3: 1953–1960.
19. Pell, W. G. and Conway, B. E. (2004) Peculiarities and requirements of asymmetric capacitor devices based on combination of capacitor and battery-type electrodes, *J. Power Sources,* 136: 334–345. doi:10.1016/j.jpowsour.2004.03.021.
20. Huang, X., Qi, X., Boey, F., and Zhang, H. (2012) Graphene-based composites, *Chem. Soc. Rev.*, 41: 666–686.
21. Plonska-Brzezinska, M. E. and Echegoyen, L. (2013) Carbon nano-onions for supercapacitor electrodes: Recent developments and applications, *J. Mater. Chem. A.*, 1: 13703. doi:10.1039/c3ta12628e.
22. Huang, J., Sumpter, B. G., Meunier, V., Yushin, G., Portet, C., and Gogotsi, Y. (2010) Curvature effects in carbon nanomaterials: Exohedral versus endohedral supercapacitors, *J. Mater. Res.*, 25: 1525–1531.
23. Portet, C., Yushin, G., and Gogotsi, Y. (2007) Electrochemical performance of carbon onions, nanodiamonds, carbon black and multiwalled nanotubes in electrical double layer capacitors, *Carbon*, 45: 2511–2518. doi:10.1016/j.carbon.2007.08.024.
24. Portet, C., Chmiola, J., Gogotsi, Y., Park, S., and Lian, K. (2008) Electrochemical characterizations of carbon nanomaterials by the cavity microelectrode technique, *Electrochimica Acta*, 53: 7675–7680.
25. Pech, D., Brunet, M., Durou, H., Huang, P., Mochalin, V., Gogotsi, Y., Taberna, P.-L., and Simon, P. (2010) Ultrahigh-power micrometre-sized supercapacitors based on onion-like carbon, *Nat. Nanotechnol.,* 5: 651–654. doi:10.1038/nnano.2010.162.
26. Presser, V., Heon, M., and Gogotsi, Y. (2011) Carbide-derived carbons–from porous networks to nanotubes and graphene, *Adv. Funct. Mater.,* 21: 810–833.
27. Al-Jishi, R. and Dresselhaus, G. (1982) Lattice-dynamical model for graphite, *Phys. Rev. B.,* 26: 4514–4522. doi:10.1103/PhysRevB.26.4514.
28. Sek, S., Breczko, J., Plonska-Brzezinska, M. E., Wilczewska, A. Z. and Echegoyen, L. (2013) STM-Based molecular junction of carbon nano-onion, *Chem. Phys. Chem.*, 14: 96–100. doi:10.1002/cphc.201200624.
29. Wang, M.-S., Golberg, D., and Bando, Y. (2010) Carbon "onions" as point electron sources, *ACS Nano*., 4: 4396–4402.
30. Gao, Y., Zhou, Y. S., Qian, M., He, X. N., Redepenning, J., Goodman, P., Li, H. M., Jiang, L., and Lu, Y. F. (2013) Chemical activation of carbon nano-onions for high-rate supercapacitor electrodes, *Carbon*, 51: 52–58. doi:10.1016/j.carbon.2012.08.009.
31. Plonska-Brzezinska, M. E., Lewandowski, M., Błaszyk, M., Molina-Ontoria, A., Luciński, T., and Echegoyen, L. (2012) Preparation and Characterization of Carbon Nano-Onion/PEDOT:PSS Composites, *Chem. Phys. Chem.,* 13: 4134–4141. doi:10.1002/cphc.201200789.
32. Breczko, J., Winkler, K., Plonska-Brzezinska, M. E., Villalta-Cerdas, A., and Echegoyen, L. (2010) Electrochemical properties of composites containing small carbon nano-onions and solid polyelectrolytes, *J. Mater. Chem.,* 20: 7761. doi:10.1039/c0jm01213k.
33. Keller, N., Maksimova, N. I., Roddatis, V. V., Schur, M., Mestl, G., Butenko, Y. V., Kuznetsov, V. L., and Schlögl, R. (2002) The catalytic use of onion-like carbon materials for styrene synthesis by oxidative dehydrogenation of ethylbenzene, *Angew. Chem. Int. Ed.,* 41: 1885. doi:10.1002/1521-3773(20020603)41:11<1885::AID-ANIE1885>3.0.CO;2-5.
34. Gu, W., Peters, N., and Yushin, G. (2013) Functionalized carbon onions, detonation nanodiamond and mesoporous carbon as cathodes in Li-ion electrochemical energy storage devices, *Carbon*, 53: 292–301.
35. Koudoumas, E., Kokkinaki, O., Konstantaki, M., Couris, S., Korovin, S., Detkov, P., Kuznetsov, V., Pimenov, S., and Pustovoi, V. (2002) Onion-like carbon and diamond nanoparticles for optical limiting, *Chem. Phys. Lett.,* 357: 336–340. doi:10.1016/S0009-2614(02)00557-2.
36. Tomita, S., Fujii, M., and Hayashi, S. (2002) Optical extinction properties of carbon onions prepared from diamond nanoparticles, *Phys. Rev. B.,* 66: 245424.
37. Joly-Pottuz, L., Matsumoto, N., Kinoshita, H., Vacher, B., Belin, M., Montagnac, G., Martin, J. M., and Ohmae, N. (2008) Diamond-derived carbon onions as lubricant additives, *Tribol. Int.,* 41: 69–78. doi:10.1016/j.triboint.2007.05.001.
38. Hirata, A., Igarashi, M., and Kaito, T. (2004) Study on solid lubricant properties of carbon onions produced by heat treatment of diamond clusters or particles, *Tribol. Int.,* 37: 899–905. doi:10.1016/j.triboint.2004.07.006.
39. Kuznetsov, V. L., Zilberberg, I. L., Butenko, Y. V., Chuvilin, A. L., and Segall, B. (1999) Theoretical study of the formation of closed curved graphite-like structures during annealing of diamond surface, *J. Appl. Phys.,* 86: 863–870.
40. Breczko, J., Plonska-Brzezinska, M. E., and Echegoyen, L. (2012) Electrochemical oxidation and determination of dopamine in the presence of uric and ascorbic acids using a carbon nano-onion and poly(diallyldimethylammonium chloride) composite, *Electrochimica Acta,* 72: 61–67. doi:10.1016/j.electacta.2012.03.177.
41. Palkar, A., Melin, F., Cardona, C. M., Elliott, B., Naskar, A. K., Edie, D. D., Kumbhar, A., Echegoyen, L. (2007) Reactivity differences between carbon nano onions (CNOs) prepared by different methods, *Chem. – Asian J.,* 2: 625–633. doi:10.1002/asia.200600426.
42. Wang, M., Ni, Y., Cao, L., Zhao, D., and Ma, X. (2013) Porous Ni/β-Ni (OH) 2 superstructures: rapid solvothermal synthesis, characterization, and electrochemical property, *J. Colloid Interface Sci.,* 401: 8–13.
43. Plonska-Brzezinska, M. E., Brus, D. M., Molina-Ontoria, A., Echegoyen, L. (2013) Synthesis of carbon nano-onion and nickel hydroxide/oxide composites as supercapacitor electrodes, *RSC Adv.,* 3: 25891. doi:10.1039/c3ra44249g.
44. Yan, H., Bai, J., Wang, J., Zhang, X., Wang, B., Liu, Q., and Liu, L. (2013) Graphene homogeneously anchored with Ni (OH) 2 nanoparticles as advanced supercapacitor electrodes, *Cryst. Eng. Comm*., 15: 10007–10015.
45. Li, Y., Li, W., Chou, S., and Chen, J. (2008) Synthesis, characterization and electrochemical properties of aluminum-substituted alpha-Ni (OH) 2 hollow spheres, *J. Alloys Compd.,* 456: 339–343.
46. Zhang, S. and Zeng, H. C. (2009) Self-assembled hollow spheres of β-Ni (OH) 2 and their derived nanomaterials, *Chem. Mater.,* 21: 871–883.
47. Xing, W., Li, F., Yan, Z., and Lu, G. Q. (2004) Synthesis and electrochemical properties of mesoporous nickel oxide, *J. Power Sources,* 134: 324–330.
48. Chmiola, J., Yushin, G., Gogotsi, Y., Portet, C., Simon, P., Taberna, P.-L. (2006) Anomalous increase in carbon capacitance at pore sizes less than 1 nanometer, *Science,* 313: 1760–1763.

49. Barrett, E. P., Joyner, L. G., and Halenda, P. P. (1951) The determination of pore volume and area distributions in porous substances. I. Computations from nitrogen isotherms, *J. Am. Chem. Soc.,* 73: 373–380.
50. Frackowiak, E. (2007) Carbon materials for supercapacitor application, *Phys. Chem. Chem. Phys.,* 9: 1774–1785.
51. Kinoshita, K. and Bett, J. A. S. (1975) Influence of electrochemical treatment in phosphoric acid on the wettability of carbons, *Carbon,* 13: 405–409.
52. Cheng, J. P., Zhang, J., and Liu, F. (2014) Recent development of metal hydroxides as electrode material of electrochemical capacitors, *RSC Adv.,* 4: 38893–38917.
53. Vidhyadharan, B., Zain, N. K. M., Misnon, I. I., Aziz, R. A., Ismail, J., Yusoff, M. M., and Jose, R. (2014) High performance supercapacitor electrodes from electrospun nickel oxide nanowires, *J. Alloys Compd.,* 610: 143–150. doi:10.1016/j.jallcom.2014.04.211.
54. Barnard, R., Randell, C. F., and Tye, F. L. (1980) Studies concerning charged nickel hydroxide electrodes I. Measurement of reversible potentials, *J. Appl. Electrochem.,* 10: 109–125.
55. Meher, S. K., Justin, P., and Rao, G. R. (2011) Nanoscale morphology dependent pseudocapacitance of NiO: Influence of intercalating anions during synthesis, *Nanoscale*, 3: 683–692. doi:10.1039/C0NR00555J.
56. Augustyn, V., Simon, P., and Dunn, B. (2014) Pseudocapacitive oxide materials for high-rate electrochemical energy storage, *Energy Environ. Sci.,* 7: 1597–1614.
57. Chang, B.-Y. and Park, S.-M. (2010) Electrochemical impedance spectroscopy, *Annu. Rev. Anal. Chem.,* 3: 207–229.
58. Hu, C.-C. and Chu, C.-H. (2001) Electrochemical impedance characterization of polyaniline-coated graphite electrodes for electrochemical capacitors—effects of film coverage/thickness and anions, *J. Electroanal. Chem.*, 503: 105–116.
59. Ganesh, V., Pitchumani, S., and Lakshminarayanan, V. (2006) New symmetric and asymmetric supercapacitors based on high surface area porous nickel and activated carbon, *J. Power Sources,* 158: 1523–1532.
60. Yoon, S.-B., Jegal, J.-P., Roh, K. C., and Kim, K.-B. (2014) Electrochemical impedance spectroscopic investigation of sodium ion diffusion in MnO2 using a constant phase element active in desired frequency ranges, *J. Electrochem. Soc.,* 161: H207–H213. doi:10.1149/2.046404jes.
61. Rouis, A., Mlika, R., Davenas, J., Ouada, H. B., Bonnamour, I., and Jaffrezic, N. (2007) Impedance spectroscopic investigations of ITO modified by new Azo-calix [4]arene immobilised into electroconducting polymer (MEHPPV), *J. Electroanal. Chem.,* 601: 29–38.
62. Han, J., Dou, Y., Zhao, J., Wei, M., Evans, D. G., and Duan, X. (2013) Flexible CoAl LDH@ PEDOT core/shell nanoplatelet array for high-performance energy storage, *Small,* 9: 98–106.
63. Sharma, R. K., Karakoti, A., Seal, S., and Zhai, L. (2010) Multiwall carbon nanotube-poly (4-styrenesulfonic acid) supported polypyrrole/manganese oxide nano-composites for high performance electrochemical electrodes, *J. Power Sources*, 195: 1256–1262.